

A Modified Model for the Lobula Giant Movement Detector and Its FPGA Implementation

Hongying Meng^a Kofi Appiah^a Shigang Yue^a Andrew Hunter^a
Mervyn Hobden^b Nigel Priestley^b Peter Hobden^b Cy Pettit^b

^a*School of Computer Science, University of Lincoln, UK*

^b*E2V Technologies PLC, Lincoln, UK.*

Abstract

Bio-inspired vision sensors are particularly appropriate candidates for navigation of vehicles or mobile robots due to their computational simplicity, allowing compact hardware implementations with low power dissipation. The Lobula Giant Movement Detector (LGMD) is a wide-field visual neuron located in the Lobula layer of the Locust nervous system. The LGMD increases its firing rate in response to both the velocity of an approaching object and the proximity of this object. It has been found that it can respond to looming stimuli very quickly and trigger avoidance reactions. It has been successfully applied in visual collision avoidance systems for vehicles and robots. This paper introduces a modified neural model for LGMD that provides additional depth direction information for the movement. The proposed model retains the simplicity of the previous model by adding only a few new cells. It has been simplified and implemented on a Field Programmable Gate Array (FPGA), taking advantage of the inherent parallelism exhibited by the LGMD, and tested on real-time video streams. Experimental results demonstrate the effectiveness as a fast motion detector.

Key words: Neural networks, Bio-inspired vision chip, Embedded vision, Visual motion, FPGA

1 Introduction

For animals, such as insects, the ability to detect approaching objects is important, serving both to prevent collision as the animal moves and also to avoid capture by predators [1,2]. Evolved over millions of years, the visual collision avoidance systems in insects are both efficient and reliable. The neural circuits processing visual information in insects are relatively simple compared

7 to those in the human brain and provide an appropriate model for the op-
8 tical collision avoidance sensors that are needed to equip mobile intelligent
9 machines [3].

10 The Lobula Giant Movement Detector (LGMD) is a wide-field visual neu-
11 ron located in the Lobula layer of the Locust nervous system. The LGMD
12 increases its firing rate in response to both the velocity of the approaching
13 object and its proximity. It responds to looming stimuli very quickly and can
14 trigger avoidance reactions when a rapidly approaching object is detected.
15 It is tightly tuned to respond to objects approaching on a direct collision
16 course [4], but produces little or no response to receding objects [5]. This
17 makes the LGMD an ideal model to develop specialized sensors for automatic
18 collision avoidance [6,7].

19 A functional neural network based on the LGMD's input circuitry was de-
20 veloped by Rind and Bramwell [8]. This neural network showed the same
21 selectivity as the LGMD neuron for approaching rather than receding objects
22 and responded best to objects approaching on collision rather than near-miss
23 trajectories. The expanding edges of colliding objects and the use of lateral
24 inhibition were the key features of the model. This neural network has also
25 been used to mediate collision avoidance in a real-world environment by in-
26 corporating it into the control structure of a miniature mobile robot [9,10].

27 Inspired by the presence of direction selective neurons in the locust [11,12],
28 a new specialized translation-sensitive neural network (TSNN) has been pro-
29 posed in [13,14]. The TSNN neuron has some common layers with the LGMD
30 model, allowing efficiency savings in the neural computation. The TSNN fuses
31 extracted visual motion cues from several whole-field direction selective neural
32 networks, and is only sensitive to translational movements.

33 TSNN can detect the direction of translation movements very well, but it
34 is not sensitive to movement in depth; LGMD [8,15] detects the direction
35 of movement in depth by both lateral inhibition and feed forward inhibition,
36 where feed forward inhibition plays a critical role in inhibiting LGMD spikes to
37 receding objects. This use of feed forward inhibition can make the system over-
38 sensitive to background movements, thus decreasing the overall sensitivity of
39 LGMD. In this paper we propose a modified model for LGMD with several
40 extra cells to capture the directional information for depth movements quickly,
41 while the feed forward inhibition cell is only responsible for whole field image
42 movements. The new model is efficiently implemented on FPGA. We have
43 previously presented preliminary details of the new model [16], but without
44 the full discussion or the FPGA implementation presented here.

45 The rest of this paper is organized as follows: In section 2, we give an overview
46 of related work. In section 3, we address the modified LGMD model and its

47 software simulation. In section 4, we discuss the FPGA design and present ex-
48 perimental results from the hardware implementation; in section 5 we present
49 conclusions.

50 2 Related work

51 Motion sensors are presently employed in a wide variety of applications includ-
52 ing surveillance, aerospace and automotive safety control systems and navi-
53 gational systems. Motion sensors are primarily based on ultrasound, passive
54 infrared (PIR) and radar detectors. Ultrasonic motion sensors are commonly
55 used for automatic door openers and security alarms. PIR sensors are perhaps
56 the most frequently used home security sensor. Radar sensors use microwave
57 signals and detect intrusion by comparing a transmitted signal with a received
58 echo signal and detect a Doppler shifted echo.

59 Recent years, vision sensors [17] are becoming increasingly cheap and reliable,
60 and may potentially be used for a number of tasks, including collision avoid-
61 ance, navigation and object recognition. This makes it desirable to develop
62 efficient collision avoidance algorithms using visual sensors. However, collision
63 avoidance is computationally demanding, and requires a very quick response
64 from the sensor [18–20].

65 Motion patterns in 2D video imagery contain distance information about ob-
66 jects in a 3D environment [21]. An object on a collision course with the sensor
67 system displays movement in depth. There is a substantial body of literature
68 on detection of depth from vision, primarily using stereo vision [22–24], al-
69 though there is also some interesting work using monocular vision [25–27]. A
70 looming object (one moving towards the sensor) appears to expand, which sug-
71 gests using optic flow algorithms and looking for a divergent flow pattern. A
72 number of authors have suggested using optic flow to compute obstacle time-
73 to-collision from a moving robot [28–30,26,31]. However, optic flow algorithms
74 are computationally expensive, and the difficulty in estimating accurate op-
75 tic flow from real world data [32] make these insufficiently robust for general
76 applications. Alternatively some collision avoidance systems are based on the
77 fusion of vision and radar sensors [33], exploiting the advantages of each.

78 Bio-inspired vision algorithms are a particularly good candidate for collision
79 avoidance systems as they use simple, easily parallelized algorithms. Galbraith
80 et al [34] proposed a population coded algorithm, built on established models
81 of motion processing in the primate visual system, to estimate the time-to-
82 collision with improved performance over the optic flow based method. How-
83 ever, it remains computationally expensive.

84 There have been a number of attempts to design a bio-inspired neural chip
 85 based on the LGMD neural network for motion detection. This bio-inspired
 86 neural model features a particularly simple and highly parallelizable architec-
 87 ture, which may consequently be efficiently implemented on hardware, leading
 88 to low cost and low power dissipation. It provides a much quicker response
 89 that the normal monocular or stereo visual sensors.

90 Laviana et al [35] proposed a vision chip architecture based on the LGMD
 91 model described in [36] – a simplification of the model proposed in [8,1].
 92 The system includes an FPGA, a block of 100×150 6-bit retinotopic units,
 93 a controller, a 16Kbits SRAM memory block, I/O registers and some other
 94 peripherals needed for addressing, timing control, digital-to analog converters
 95 and temperature monitoring. The FPGA chip uses $0.35\mu\text{m}$ 2P-2M technology.
 96 Okuno and Yagi [37,38] implemented an LGMD model based on [8], for a
 97 real-time collision avoidance vision sensor. The system consists of an analog
 98 VLSI silicon retina and a digital FPGA circuit. The system responds selec-
 99 tively to colliding objects even in complicated real-world situations. These two
 100 implementations both use FPGA, but have some important limitations: first,
 101 they are based on the original LGMD model, which lacks movement direction
 102 information; second, both have built-in restrictions due to their tight integra-
 103 tion with the non-FPGA parts of the system (e.g. the retinotopic units), and
 104 therefore are not general purpose FPGA implementations.

105 In this paper, in order to reduce the false alarm caused by receding objects in
 106 the LGMD model, we modify the model to distinguish approaching movement
 107 from receding movement. The modified model retains simplicity in the soft-
 108 ware and hardware implementation. Its resource usage is low enough to admit
 109 integration with other functions on the FPGA, and it can be transferred to
 110 any FPGA development platform. This design can achieve a very high frame
 111 rate and can be applied in real-time vehicular collision avoidance systems with
 112 a low false alarm rate.

113 3 Modified LGMD neural network model

114 The LGMD based neural network proposed in this paper is based on previous
 115 studies described in [8,10,39,40]. The modified neural network is shown in
 116 figure 1. The LGMD neural network in [8–10] was composed of four groups
 117 of cells - photoreceptor cells (P); excitatory and inhibitory cells (E and I);
 118 summing cells (S); and two single cells for feed-forward inhibition (FFI) and
 119 LGMD. The model in [40,15] has an extra set of grouping cells between the
 120 summing cells and LGMD. This allows clusters of excitation in the summary
 121 cells to feed into the LGMD cell, which is useful for collision detection in
 122 complex backgrounds.

The input to the P cells is the luminance change. Lateral inhibition is indicated with dotted lines and has a one frame delay. Excitation is indicated with black lines and has no delay. The FFI also has a one frame delay. The input to FFI is the luminance change from the photoreceptor cells. The problem of parameter selection in this LGMD model has been tackled in [41].

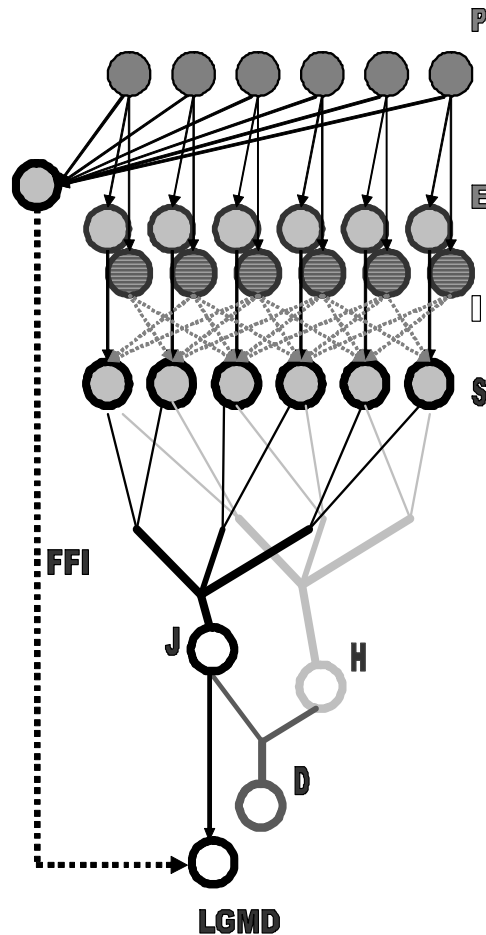


Fig. 1. A schematic illustration of the modified LGMD neural network model. There are four groups of cells and five single cells: photoreceptor cells (P); excitatory and inhibitory cells (E and I); summing cells (S); grouping cells (J and H); depth movement direction cell (D); the LGMD cell and the feed forward inhibition cell (FFI).

The model in [40] works very well for collision detection in complex environments. However, it cannot distinguish the direction of moving objects in depth. For example, it will respond to both an approaching object and a receding object with high excitation level, especially when an object is very close. To enhance the ability to recognize the direction of the moving object in depth, we add a new neural layer with two grouping cells J and H , and a

new cell D to give in-depth direction information; see figure 1. Note that the J , H and D cells may not have exact counterparts in the locust visual system. The model is described in detail below.

3.1.1 P layer

The first layer contains the photoreceptor P cells arranged in a retinotopic matrix; the input frame pixel luminance L_f is captured by each photoreceptor cell. The cells calculate the luminance change, which forms the output of this layer, using the equation:

$$P_f(x, y) = \sum_i^{n_p} p_i P_{f-i}(x, y) + (L_f(x, y) - L_{f-1}(x, y)) \quad (1)$$

where $P_f(x, y)$ is the change of luminance corresponding to pixel (x, y) at frame f , x and y are the index into the matrix, L_f and L_{f-1} are the luminance, subscript f denotes the current frame and $f - 1$ denotes the previous frame, n_p defines the maximum number of frames (or time steps) the persistence of the luminance change can last, the persistence coefficient $p_i \in (0, 1)$ and

$$p_i = (1 + e^{\mu i})^{-1} \quad (2)$$

where $\mu \in (-\infty, +\infty)$ and i indicates the previous i^{th} frame counted from the current frame f . The LGMD neural network detects potential collision by responding to expansion of the image edges, a strategy that does not rely on object appearance. If there is no difference between successive images, the P cells are not excited.

3.1.2 I E layer

The output of the P cells forms the inputs to two separate cell types in the next layer. The excitatory cells pass excitation directly to their retinotopic counterparts in the third layer, the S layer. The excitation $E(x, y)$ in an E cell has the same value as that in the corresponding P cell. The lateral inhibition cells pass inhibition, after 1 image frame delay, to their retinotopic counterpart's neighboring cells in the S layer. The inhibition strength of a cell in this layer is given by:

$$I_f(x, y) = \sum_i \sum_j P_{f-1}(x + i, y + j) w_I(i, j), \quad (if \ i = j, j \neq 0) \quad (3)$$

where $I_f(x, y)$ is the inhibition corresponding to pixel (x, y) at current frame f , $w_I(i, j)$ is the local inhibition weight. Note that i and j are not allowed

166 to be equal to zero simultaneously. Consequently, inhibition spreads out to
 167 neighboring cells in next layer rather than to the direct counterpart.

168 In our experiments, on both software simulation and hardware implementa-
 169 tion, the local inhibition weight $w_I(i, j)$ are set to 0.25 for the four nearest
 170 neighbors and 0.125 for the four diagonal neighbors. These values are espe-
 171 cially convenient for hardware implementation.

$$172 \quad w_I = \begin{bmatrix} 0.125 & 0.25 & 0.125 \\ 0.25 & & 0.25 \\ 0.125 & 0.25 & 0.125 \end{bmatrix} \quad (4)$$

173 3.1.3 *S layer*

174 The excitatory flow from the E cells and inhibition from the I cells is summed
 175 by the S cells using the following equation:

$$176 \quad S_f(x, y) = E_f(x, y) - I_f(x, y)W_I \quad (5)$$

177 where W_I is the inhibition weight (usually less than 0.8; 0.35 was empirically
 178 chosen in our experiments). Excitations that exceed a threshold value are able
 179 to reach the summation cell LGMD:

$$180 \quad \tilde{S}_f(x, y) = \begin{cases} S_f(x, y), & \text{if } S_f(x, y) \geq T_r \\ 0, & \text{if } S_f(x, y) < T_r \end{cases} \quad (6)$$

181 where T_r is the threshold.

182 3.1.4 *J H cells*

183 The J and H cells are the two new grouping cells for depth movement direction
 184 recognition. The J cell is exactly the same as the LGMD cell in the previous
 185 LGMD model in terms of spatiotemporal structure and the value it holds: it
 186 sums the S cell activations to give an overall network response. The H cell
 187 shares the same structure as J cell, but with a temporal difference, having a
 188 one frame delay from J .

$$189 \quad J_f = \sum_{x,y} \tilde{S}_f(x, y) \quad (7)$$

$$190 \quad H_f = J_{f-1} \quad (8)$$

191 From equations 1,3,5 and 7 it can be seen that the value of the J cell is
 192 particularly sensitive to pixels where there is a luminance changes between
 193 consecutive frames.

194 3.1.5 D cell

195 The D cell is used to calculate the difference between the differences of frame
 196 f , $f - 1$ and $f - 2$. It can be represented in the equation 9.

$$197 \quad D_f = abs(J_f) - abs(H_f) \quad (9)$$

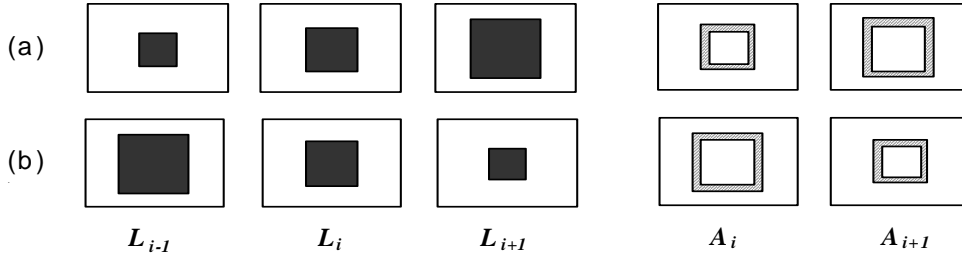


Fig. 2. An illustration of the difference between approaching (a) and receding (b) depth movement. L_{i-1} , L_i and L_{i+1} are three consecutive three frames in the video clip. A_i and A_{i+1} are the affected areas while doing the frame subtractions between these frames. In the approaching case, the affected area gets larger; in the receding case smaller.

198 The D cell estimates the direction of movement in depth very well. It exploits
 199 the property that a looming object gets larger, whereas a receding one gets
 200 smaller; see figure 2. Due to the aperture effect, a moving object may only
 201 cause detectable changes around the edge (or internal contrast boundaries);
 202 however, at constant speed the size of the area of change is still related to the
 203 direction of movement in depth. When an object is moving away, $abs(J_f)$ is
 204 smaller than $abs(H_f)$. When an object is approaching, $abs(J_f)$ is bigger than
 205 $abs(H_f)$. The absolute value function on J and H cells is used to cancel the
 206 different effects on their values when the object is darker or brighter than the
 207 background. In order to distinguish slow movements we add a threshold T_D
 208 for D_f . We then get a simple variable \tilde{D} that has only three values: '0', '1'
 209 and '-1', where '1' stands for approaching, '-1' for receding and '0' for no
 210 significant movement. The threshold T_D depends mainly on the size of the
 211 image.

$$212 \quad \tilde{D}_f = \begin{cases} 1, & \text{if } D_f \geq T_D \\ 0, & \text{if } -T_D < D_f < T_D \\ -1, & \text{if } D_f \leq -T_D \end{cases} \quad (10)$$

213 When augmented with the above cells, the LGMD model recognizes directional
 214 information for depth movements quickly. The feed forward inhibition cell, as
 215 detailed later, is able to concentrate on whole image movements to avoid
 216 perturbation from background movements.

217 3.1.6 LGMD cell

218 The membrane potential J is then transformed to a spiking output using a
 219 sigmoid transformation,

$$220 \quad LGMD_f = (1 + e^{-J_f n_{cell}^{-1}})^{-1} \quad (11)$$

221 where n_{cell} is the total number of the cells in S layer. Since J_f is greater than
 222 or equal to zero (as equation 7 is a sum of absolute value), the sigmoid mem-
 223 brane potential $LGMD_f$ varies from 0.5 to 1. The collision alarm is decided
 224 by the spiking of cell LGMD. If the membrane potential $LGMD_f$ exceeds the
 225 threshold T_s , a spike is produced. A certain number of successive spikes, de-
 226 noted by S_{LGMD} , will trigger the collision alarm in the LGMD cell. Of course,
 227 in the modified model, the collision alarm is only triggered under the condi-
 228 tion that $\tilde{D} = 1$ where the moving object is approaching. The spikes may be
 229 suppressed by the FFI cell when whole field movement occurs [39].

230 3.1.7 FFI cell

231 If it is not suppressed during turning, the network may produce spikes and
 232 even false collision alerts due to sudden changes in the scene. The feed forward
 233 inhibition and lateral inhibition work together to cope with such whole field
 234 movement [39]. The FFI excitation at the current frame is gathered from the
 235 photoreceptor cells with one frame delay,

$$236 \quad F_f = \sum_j^{n_a} \alpha_{f-j}^F F_{f-j} + \sum_{x=1}^{n_r} \sum_{y=1}^{n_c} abs(P_{f-1}(x, y)) n_{cell}^{-1} \quad (12)$$

237 where α_{f-j}^F is the persistence coefficient for FFI and $\alpha_{f-j}^F \in (0, 1)$, n_a defines
 238 how many time steps the persistence can last.

239 Once F_f exceeds its threshold T_{FFI} , spikes in the LGMD are inhibited imme-
 240 diately. The threshold T_{FFI} is also adaptable,

$$241 \quad T_{FFI} = T_{FO} + \alpha_{ffi} T_{FFI_{f-1}} \quad (13)$$

where T_{FO} is the initial value of the T_{FFI} , the adaptable threshold is decided by the previous T_{FFI} and α_{ffi} is a coefficient. The parameters, including T_{FO} , α_{ffi} , are tuned to the application, the value depending on the image size and the style of camera movement. In the case when the camera is nearly stable, the FFI cell is normally ignored as it rarely reacts.

3.2 Simulation results on the proposed model

Two data sets were used to test the efficiency and stability of the proposed LGMD model in software simulation. The first experiment is on a simulated data set that demonstrates carefully-calibrated approaching and receding movements. The second data sets are two recorded video clips. The parameters were kept the same in all experiments; values are shown in table X. [YOU BEST REPLACE THIS X!]. The simulation was performed using MATLAB. Because the camera was still in the following experiments, FFI cell was ignored. Other parameters used in the all following experiments are listed in the table 1

Table 1

Settings for the control parameters of the LGMD model where n_r and n_c are the numbers of the pixels in the horizontal and vertical directions in the video frame.

n_p	μ	p_1	W_I	T_r	T_D	n_{cell}
1	1.95	0.125	0.25	3	$0.25 * n_r * n_c$	$n_r * n_c$

3.2.1 Results on simulated data set

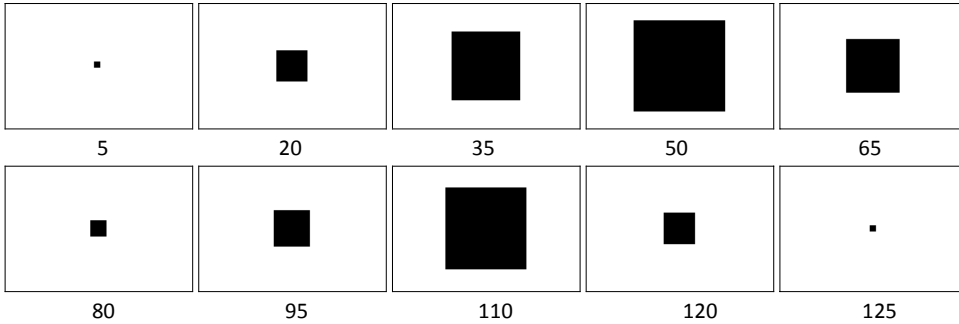


Fig. 3. Selected frames from the simulated sequence. The square object looms and recedes twice, with the second sequence at twice the speed of the first.

We created a sequence containing 125 frames, resolution 150×100 , of a square black object on a white background. The object alternatively approaches and recedes. Sample frames are shown in figure 3. Initially the square is stationary with size 3×3 . It looms from frame 5 – 41, then recedes from frame 41 – 79,

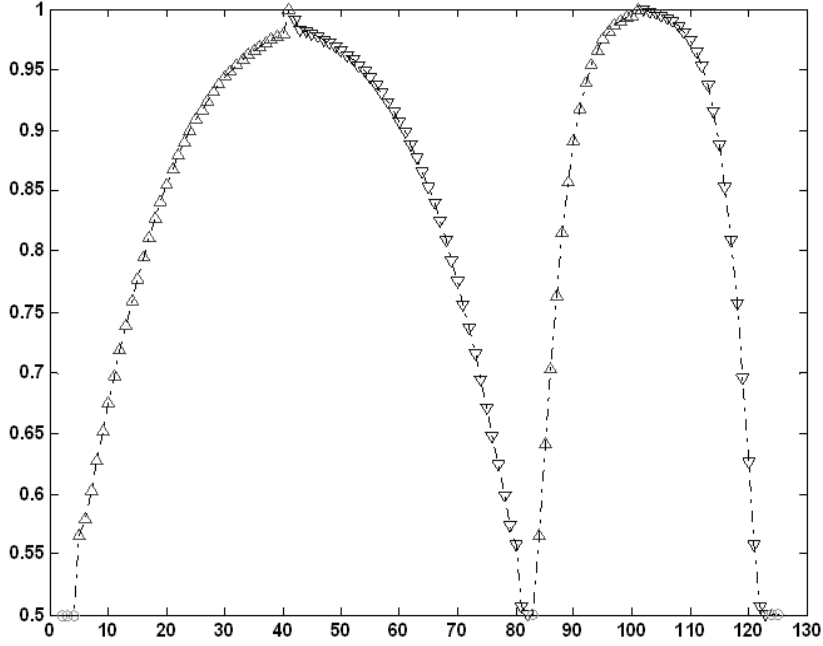


Fig. 4. Output of the new LGMD model on the simulated sequence shown in figure 3. The vertical axis shows the normalized membrane potentials of the LGMD cell; the markers denote the depth movement direction of the object: ‘ \triangle ’ denotes approaching, ‘ ∇ ’ receding and ‘ \circ ’ no significant movement.

both at one pixel per side per frame. It is stationary from frames 79 – 84, at size 3×3 , then approaches from 84 – 101 and recedes from 101 – 120, this time at 2 pixels per edge per frame. It remains stationary again at size 3×3 for the remainder of the sequence.

Figure 4 shows the output of the LGMD model on the simulated sequence shown in figure 3. The vertical axis is the normalized membrane potential of the LGMD cell; the marker represents the output of the depth direction cell. This result shows that this model works very well in the simulation dataset.

3.2.2 Results on real recorded data

We recorded two short video clips (shown in figures 5 and 7 respectively) for the second experiment, using 320×240 gray scale images. In these videos (5) a ball is shown, mainly receding to the chair and then bouncing back to approach the camera. There are 18 and 21 frames in the first and second sequences respectively. The first recording has a bigger, fast-moving ball while the second has a smaller, slower-moving ball.

Figure 6 and 8 show the output of the new model on the recorded sequences shown in figure 5 and 7 respectively. In the first dataset, the ball is a bit brighter than background while in the second dataset, the ball is a bit darker than the background. Although the situations are different, the simulation

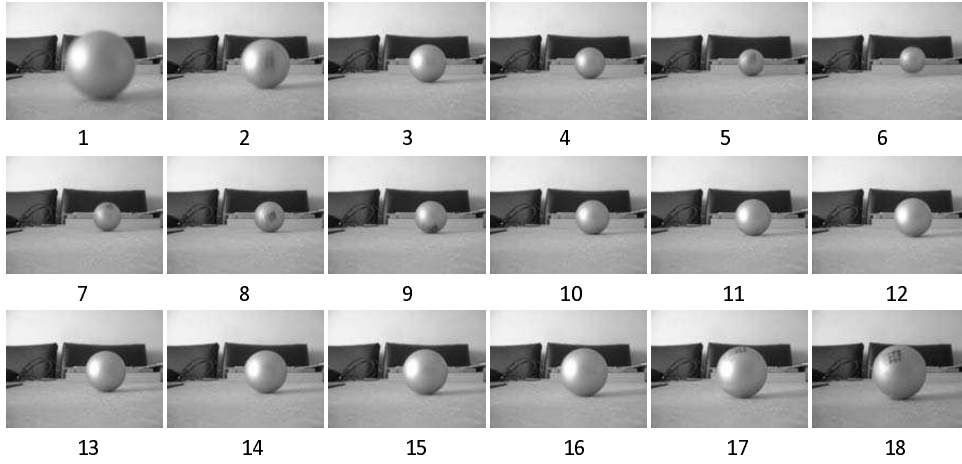


Fig. 5. The first recorded sequence. There are 18 frames featuring a ball receding from the camera and then bouncing back to the camera after it hits a chair.

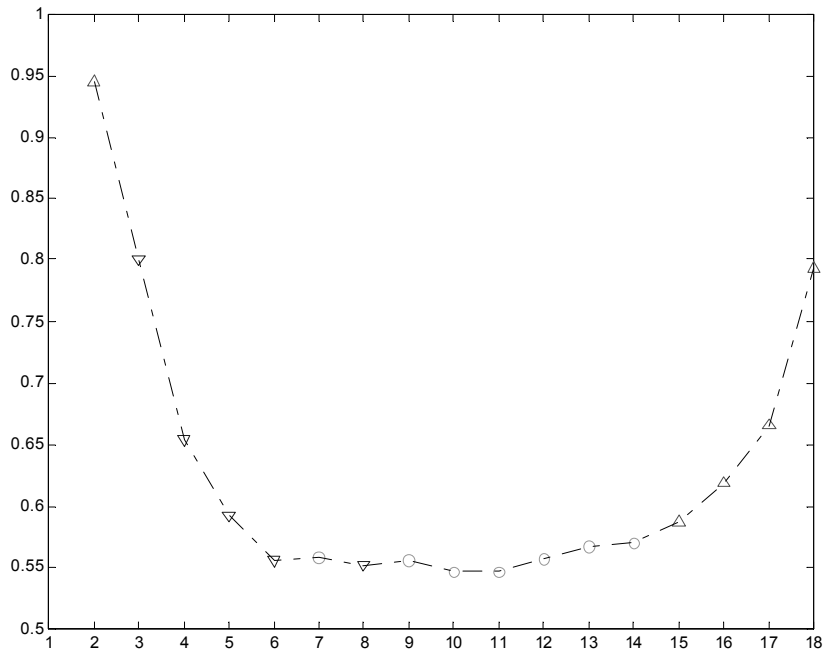


Fig. 6. The output of the model on the sequence shown in figure 5. The vertical axis is the normalized membrane potentials of the LGMD cell. The markers denote the depth movement direction; '△' denote approaching objects; '▽' receding objects and '○' no significant movement.

281 results are quite similar. We can clearly see that the new model works very
 282 well on both recorded data sets.

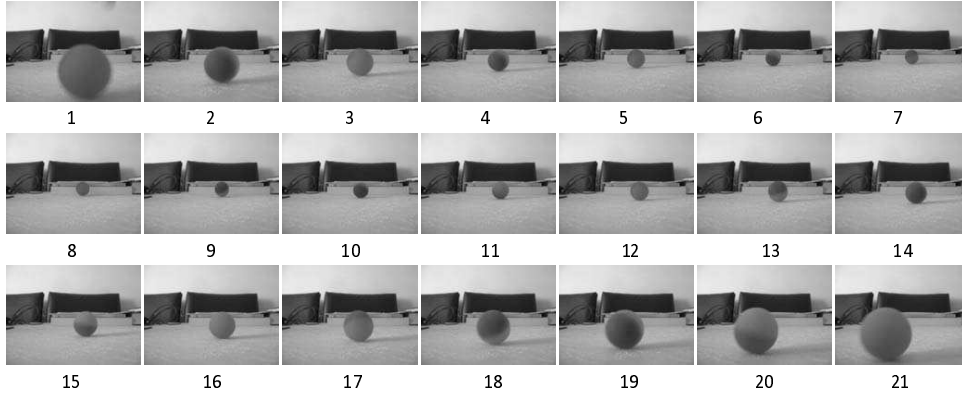


Fig. 7. The second recorded sequence. There are 21 frames, featuring a ball receding from the camera and then bouncing back towards the camera after it hits the chair.

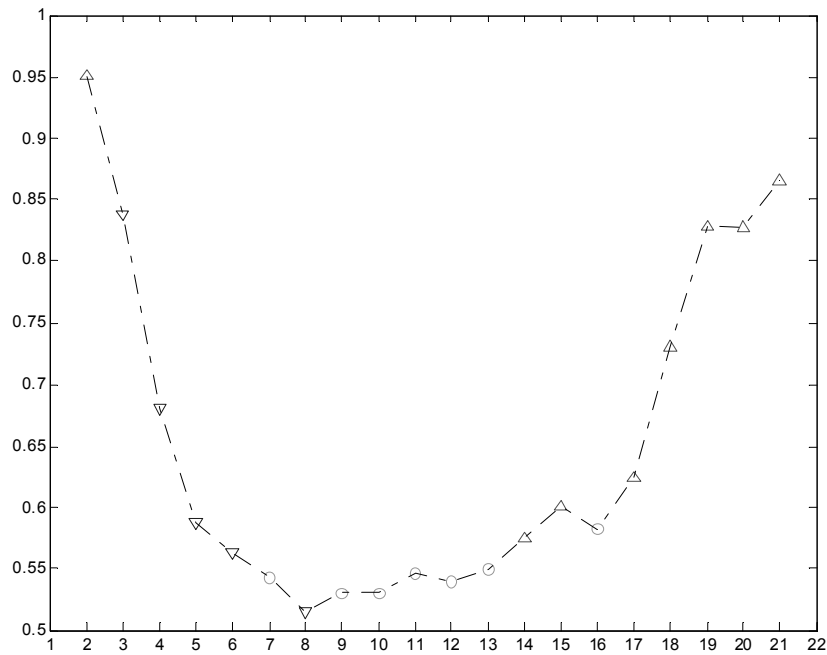


Fig. 8. The output of the model on the sequence shown in figure 7. The vertical axis is the normalized membrane potentials of the LGMD cell. The markers denote the depth movement direction; '△' denote approaching objects; '▽' receding objects and '○' no significant movement.

283 4 Hardware design and implementation

284 The entire collision detection algorithm, based on the modified LGMD as
 285 presented in section 3 has been implemented on a Field Programmable Gate
 286 Array (FPGA). In contrast to the previously published mixed digital/analogue
 287 implementation of the LGMD[35,37], this all-digital implementation has key
 288 advantages in easy integration with other digital algorithms on the FPGA.

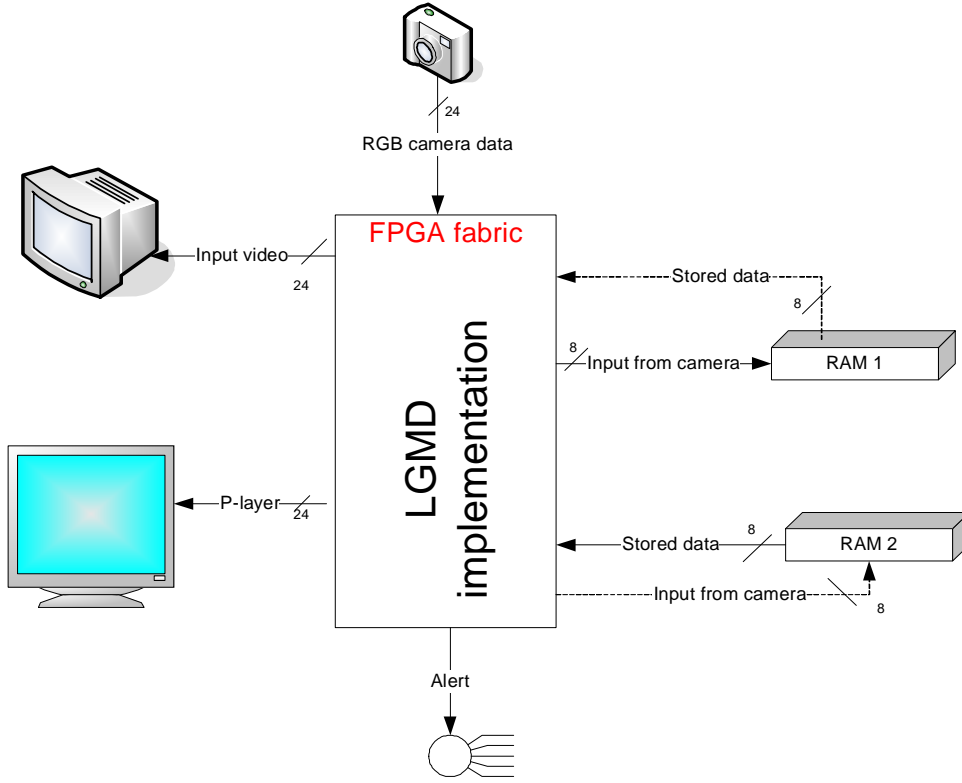


Fig. 9. A high-level block diagram of the FPGA implementation of the modified LGMD model.

4.1 Overall architecture and platform

The high-level block diagram of the overall architecture of the system is shown on figure 9. The real-time video stream is input from a digital camera to the FPGA chip, displayed on an monitor and the frames transferred to gray scale images stored in two external RAMs. The neural computing is carried out on the FPGA chip, the excitation S-layer is displayed on another monitor, and an alert is also generated.

Figure 10 shows the system setup. It includes a Celoxica RC340 board, a digital camera and two monitors. The LGMD and D cell outputs are displayed on the board's LCD, and the LEDs (flash lights) are activated on alert. The Celoxica RC340 board is packaged with a Xilinx Virtex-4 XC4VLX160, embedded Block RAM totaling 5,184 Kbits and four banks of ZBT RAM totaling 32MB, LCD, LEDs and multiple video input and output ports.



Fig. 10. The system setup includes a Celoxica RC340 board, a digital camera and two monitors. The modified LGMD model lights up the LEDs (flash lights) on the FPGA board based on the values of both LGMD and D cells. These values are also shown on the LCD of the FPGA board.

302 4.2 *FPGA design*

303 The FPGA design (see figure 11) has five blocks: the input, P-layer, S-layer, J
304 cell and D cell. The input and P-layer blocks run in parallel, while the S-layer
305 gets triggered when the entire frame has been processed.

306 The input block reads real-time camera data in 24 bit RGB format and con-
307 verts it into 8-bit gray-scale intensity. The 8-bit intensity value is written into
308 one of the available RAM blocks while the corresponding stored data is read
309 from the other RAM block, serving as the previous pixel value. The 10-bit x-
310 location and y-location address is also use to address the store data in RAM.
311 The two block of RAM are used to buffer input data from the camera.

312 The current pixel value (from the camera) and the previous pixel value (from
313 RAM) are used to estimate the luminance P-layer value for the corresponding
314 pixel. This three stage pipeline is completed when an entire frame is captured.
315 The excitatory S-layer is then triggered. This layer uses all eight neighboring
316 pixels in the P-layer. The architecture implemented here is as shown in figure
317 12. Pixel data from the three rows involved in the computation are copied
318 into a buffer one after the other. The S-layer for each pixel takes exactly three

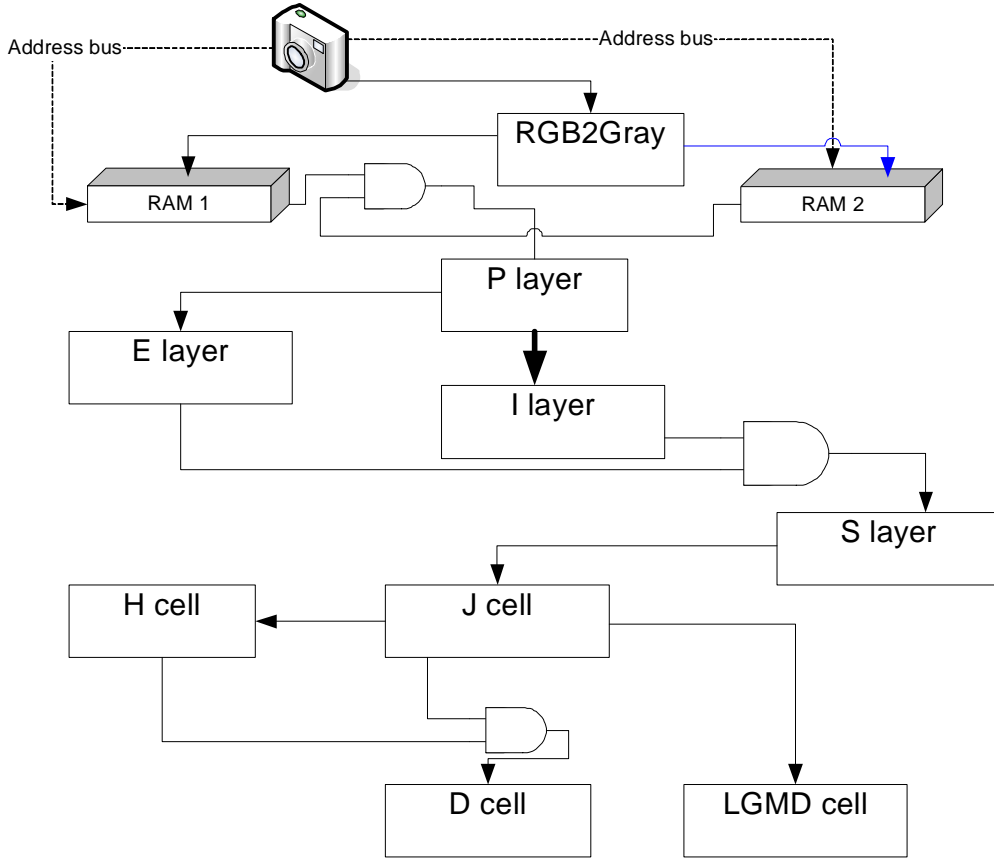


Fig. 11. A high-level circuitry diagram of the various blocks on FPGA

319 clock cycles, the same number of cycles required to fill the three buffers.

320 The processing requires seven comparators arranged in a chain as shown in
 321 figure 12 and begins execution as soon as the buffer is full. From figure 12,
 322 the shaded pixels in the second row are the pixel whose corresponding S-layer
 323 value will be generated after three clock cycles.

324 The S-layer data is passed over to the J cell, which sums all the pixels values
 325 from the S-layer. This block runs in parallel with the S-layer and uses a single
 326 accumulator. The J cell in conjunction with the H cell is used to generate the
 327 value for the D cell. The D cell uses the H cell, which is the delayed J cell
 328 value, as shown in figure 11.

329 In addition, we simulate equation 11, which determines the output of the
 330 *LGMD* cell from the input, *J*, using a step function, thus avoiding the com-
 331 putation of exponentials and division. We discretize the output, *LGMD*, into
 332 the set $\{0.50, 0.51, \dots, 0.99, 1.00\}$. Since equation 11 is monotonically increas-
 333 ing in *J*, we can rearrange equation 11 to equation 14, to back-calculate the
 334 minimum and maximum values of *J* that yield a specified value of *LGMD*
 335 (e.g. we plug values of *LGMD* = 0.505 and *LGMD* = 0.515 into 14 to cal-

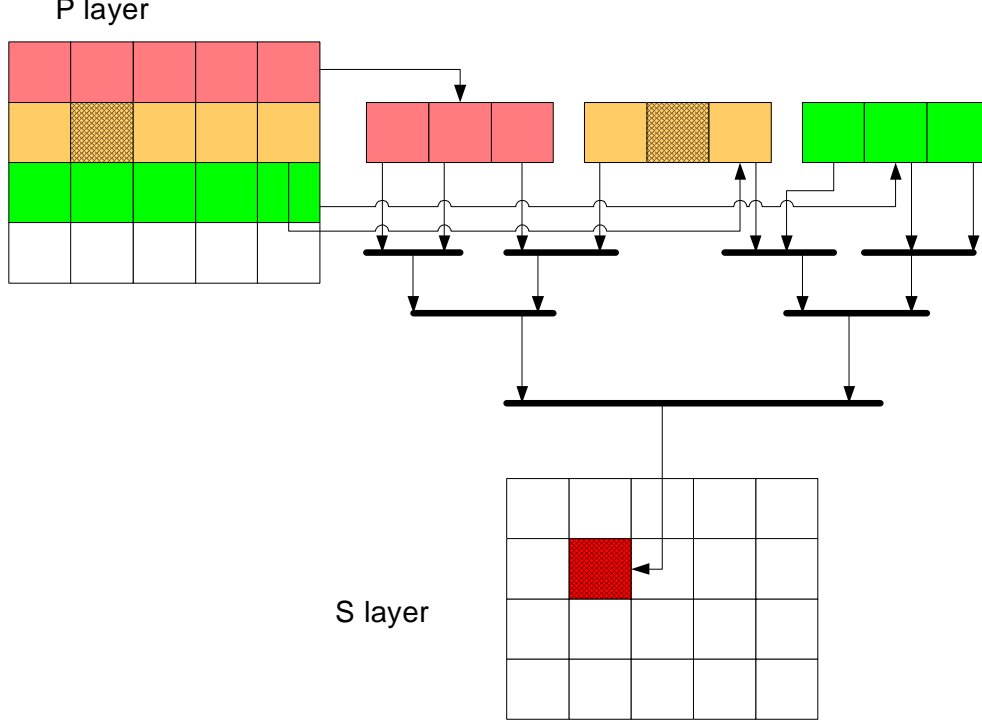


Fig. 12. A detailed translation of the p-layer into s-layer

336 culate the minimum and maximum values of J that map to $LGMD = 0.51$.
 337 These range limits are checked in parallel to determine the value of $LGMD$
 338 in a single clock cycle.

$$339 \quad J_f = -\ln(LGMD_f^{-1} - 1) \times n_{cell} \quad (14)$$

340 All the layers in the modified LGMD have been implemented on the FPGA
 341 fabric with the use of the Block RAM, making it possible to address each
 342 layer like a dual-port memory block. The hardware implementation currently
 343 excludes the FFI cell as shown in figure 1. However, this can be easily added
 344 as it is not computationally complex. The hardware implementation rather
 345 makes use of a predefined threshold to estimate the excitation. The excitation
 346 of the LGMD cell in figure 12 is very dependent on the value of the D cell;
 347 thus if the object is stationary or receding, there is no alert generated at the
 348 LGMD cell.

349 The resources used by the FPGA implementation are listed in table 2. It was
 350 implemented on a Xilinx Virtex-4 *XC4VLX160* chip, package *FF1148* and
 351 speed grade *-10*. Memory and IO requirements are high, but computational
 352 requirements are minimal.

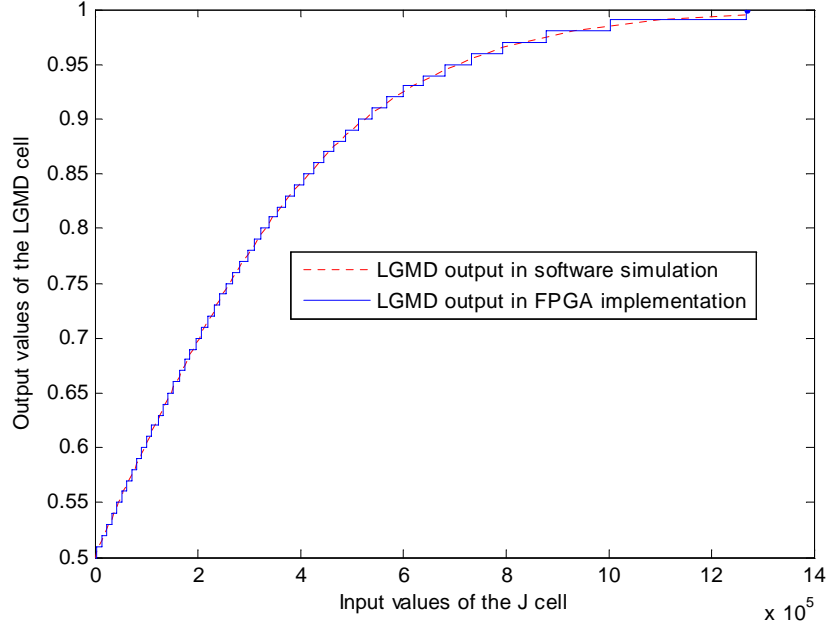


Fig. 13. A step function is used in FPGA implementations for determining the outputs of *LGMD* cell (vertical axis) from the inputs of *J* cell (horizontal axis). Only 51 values $\{0.50, 0.51, \dots, 0.99, 1.00\}$ were used for the outputs of *LGMD* cell in the FPGA implementation. Here, the image size is 600×400 .

Table 2

Implementation results for the modified LGMD, using Virtex-4 *XC4VLX160*, package *FF1148* and speed grade *-10*.

Resource		Total Used	
Name	Total	Used	Per.(%)
Flip Flops	135,168	2,325	1
4 input LUTs	135,168	3,001	2
bonded IOBs	768	355	46
Occupied Slices	67,584	3,206	4
RAM16s	288	285	98

4.3 Hardware testing results

The hardware implementation has been tested with two frame sizes, 300×200 and 600×400 . The maximum attainable clock frequency is 50MHz, with 40MHz being the highest stable frequency. The design takes a total of $3N + 7$ cycles to completely generate an LGMD output, where N is the number of pixels in the entire frame. For frame size 300×200 running at 40MHz, the system processes approximately 222 frames per second; for frame size 600×400 the value reduces to 55 frames per second. The low resource utilization of

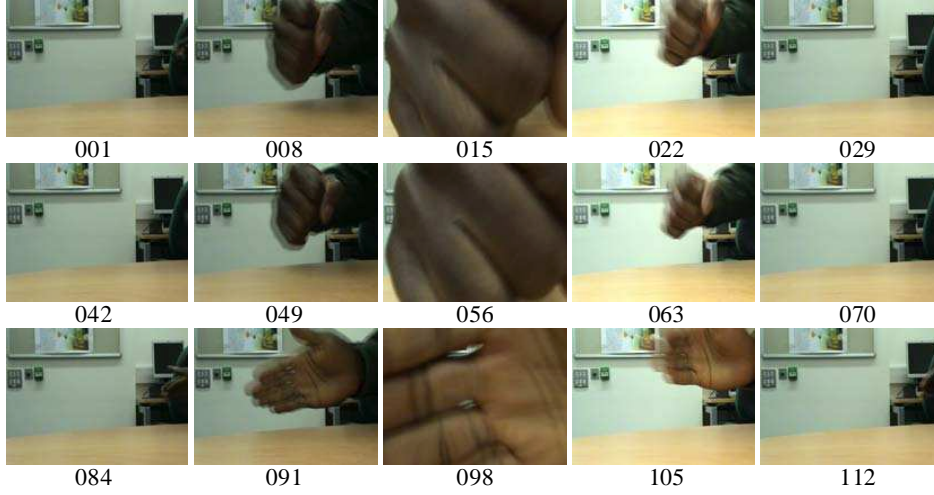


Fig. 14. Frame samples from a video clip of a looming and receding hand movement. The frame numbers are shown under each frame. There are 115 frames, size 600×400 , at frame rate 25 f.p.s.

the implementation makes it possible to run multiple LGMD at the same frequency.

The high computational efficiency makes it possible for the modified LGMD to be used in visual sensor systems with very high frame rate and/or high image resolution.

The reported clock frequency of 40MHz to 50MHz also includes the design for controlling the external logic for the 2 VGAs, the camera input and the LEDs for alerts. The design and verification was accomplished using Handel-C high level descriptive language. Compilation and simulation were achieved using the Agility DK design suite. Synthesis, the translation of abstract high-level code into a gate-level netlist, was accomplished using Xilinx ISE tools.

Figure 14 shows a video sequence used to test the hardware implementation. The object (hand) approaches and recedes three times. The video was recorded into the digital camera and the outputs of the LGMD and D cells were written into the external memory, and retrieved for plotting; see figure 15. We can see clearly that the FPGA implementation worked very well in response to this object movement. In comparison with the software simulation results (see figure 6), the curve is not as smooth, due to the step function used in the computation of the LGMD values. Nevertheless, this implementation fulfils the task of giving correct alarms.

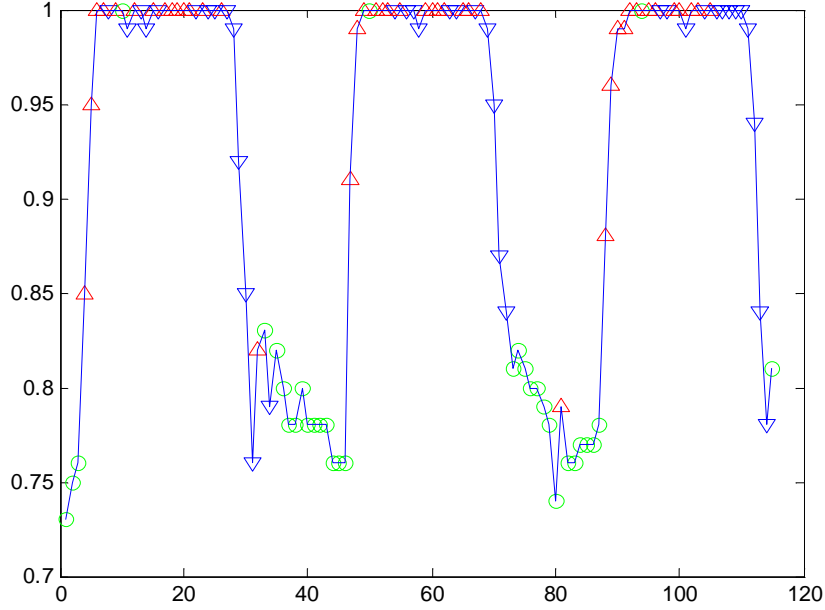


Fig. 15. Experimental results read from external memory of the FPGA board, using the video sequence in figure 14. The vertical axis is the normalized membrane potentials of the LGMD cell. The markers denote the depth movement direction; ‘ Δ ’ denote approaching objects; ‘ ∇ ’ receding objects and ‘ \bigcirc ’ no significant movement.

5 Conclusion

In this paper, we propose an LGMD model that provides additional information on the depth direction of the movement. It requires little additional computational cost compared to previous models, and can distinguish approaching from receding objects very quickly.

The new model has been implemented on the Xilinx FPGA chip, and the general purpose design is suitable for transfer to any other FPGA device. The design is compact, occupying limited hardware resources, and therefore be easily integrated with other computational components on a single chip. It has been successfully tested on real-time video clips; experimental results showed hardware performance is consistent with software simulation results.

The high computational efficiency makes the modified LGMD suitable for use in visual sensor systems with very high frame rate and/or high image resolution, and the implementation on a general purpose hardware platform makes it suitable for application in various situations.

In future research we will design a complete chip combining this LGMD model with the specialized translation-sensitive neural network. This will provide both translation and depth movement information, and will work as a general motion tracking sensor.

400 6 Acknowledgments

401 The authors would like to thank the UK Trade and Strategy Board for sup-
402 porting the project under the program grant TP/2/SC/6/I/10444.

403 References

- 404 [1] F. C. Rind, P. J. Simmons, Seeing what is coming: building collision-sensitive
405 neurones., *Trends in Neurosciences* 22 (1999) 215–220.
- 406 [2] R. D. Santer, P. J. Simmons, F. C. Rind, Gliding behaviour elicited by
407 lateral looming stimuli in flying locusts., *Journal of comparative physiology.*
408 A, *Neuroethology, sensory, neural, and behavioral physiology* 191 (1) (2005)
409 61–73.
- 410 [3] F. C. Rind, R. D. Santer, M. J. Blanchard, P. F. M. J. Verschure, *Locust looming*
411 *detectors for robot sensors*, Springer, Berlin, 2003.
- 412 [4] S. Judge, F. C. Rind, The locust DCMD, a movement-detecting neurone tightly
413 tuned to collision trajectories, *Journal of Experimental Biology* 200 (16) (1997)
414 2209–2216.
- 415 [5] F. C. Rind, P. J. Simmons, Orthopteran DCMD neuron: a reevaluation of
416 responses to moving objects. I. selective responses to approaching objects, *J*
417 *Neurophysiol* 68 (5) (1992) 1654–1666.
- 418 [6] S. B. i Badia, P. F. Verschure, A collision avoidance model based on the lobula
419 giant movement detector neuron of the locust, in: *proceedings of IJCNN, 2004*,
420 pp. 1757–1761.
- 421 [7] S. Bermudez i Badia, P. Pyk, P. F. Verschure, A fly-locust based neuronal
422 control system applied to an unmanned aerial vehicle: the invertebrate neuronal
423 principles for course stabilization, altitude control and collision avoidance, *The*
424 *International Journal of Robotics Research* 26 (7) (2007) 759–772.
- 425 [8] F. Rind, D. Bramwell, Neural network based on the input organization of an
426 identified neuron signaling impending collision., *Journal of Neurophysiology* 75
427 (1996) 967–985.
- 428 [9] M. Blanchard, P. F. M. J. Verschure, F. C. Rind, Using a mobile robot to study
429 locust collision avoidance responses, *Int. J. Neural Syst.* 9 (5) (1999) 405–410.
- 430 [10] M. Blanchard, F. Rind, P. Verschure, Collision avoidance using a model of the
431 locust LGMD neuron., *Robotics and Automonous Systems* 30 (2000) 17–38.
- 432 [11] F. C. Rind, A directionally selective motion-detecting neurone in the brain
433 of the locust: physiological and morphological characterization, *Journal of*
434 *Experimental Biology* 149 (1990) 1–19.

- 435 [12] F. C. Rind, Identification of directionally selective motion-detecting neurones in
436 the locust lobula and their synaptic connections with an identified descending
437 neurone, *Journal of Experimental Biology* 149 (1990) 21–43.
- 438 [13] S. Yue, F. C. Rind, Visual motion pattern extraction and fusion for
439 collision detection in complex dynamic scenes, *Computer Vision and Image*
440 *Understanding* 104 (1) (2006) 48 – 60.
- 441 [14] S. Yue, F. C. Rind, A synthetic vision system using directionally selective
442 motion detectors to recognize collision, *Artificial Life* 13 (2) (2007) 93–122.
- 443 [15] S. Yue, F. C. Rind, Collision detection in complex dynamic scenes using
444 an LGMD-based visual neural network with feature enhancement, *IEEE*
445 *Transactions on Neural Networks* 17 (3) (2006) 705–716.
- 446 [16] H. Meng, S. Yue, A. Hunter, K. Appiah, M. Hobden, N. Priestley, P. Hobden,
447 C. Pettit, A modified neural network model for lobula giant movement detector
448 with additional depth movement feature, in: *Proceedings of IJCNN, USA, 2009*,
449 pp. 2078–2083.
- 450 [17] C. Connolly, Collision avoidance technology: from parking sensors to unmanned
451 aircraft, *Sensor Review* 27 (3) (2007) 182–188.
- 452 [18] M. Bertozzi, A. Broggi, A. Fascioli, Vislab and the evolution of vision-based
453 UGVs, *IEEE Computer* 39 (12) (2006) 31–38.
- 454 [19] M. Bertozzi, L. Bombini, A. Broggi, P. Zani, P. Cerri, P. Grisleri, P. Medici,
455 Gold: A framework for developing intelligent-vehicle vision applications, *IEEE*
456 *Intelligent Systems* 23 (1) (2008) 69–71.
- 457 [20] A. Hanazawa, T. Miki, K. Horio (Eds.), *Brain-Inspired Information Technology*,
458 Vol. 266 of *Studies in Computational Intelligence*, Springer, 2010.
- 459 [21] H. Longuet Higgins, K. Prazdny, The interpretation of a moving retinal image,
460 *Proceedings of the Royal Society of London. Series B, Biological Sciences* 208
461 (1980) 385–397.
- 462 [22] G. T. Kenyon, Time-to-collision estimation from motion based on primate visual
463 processing, *IEEE Trans. Pattern Anal. Mach. Intell.* 27 (8) (2005) 1279–1291.
- 464 [23] S. Nedeveschi, S. Bota, C. Tomiuc, Stereo-based pedestrian detection
465 for collision-avoidance applications, *IEEE Trans. Intelligent Transportation*
466 *Systems* 10 (3) (2009) 380–391.
- 467 [24] A. Barth, U. Franke, Estimating the driving state of oncoming vehicles from
468 a moving platform using stereo vision, *IEEE Trans. Intelligent Transportation*
469 *Systems* 10 (4) (2009) 560–571.
- 470 [25] A. Wedel, U. Franke, J. Klappstein, T. Brox, D. Cremers, Realtime
471 depth estimation and obstacle detection from monocular video, in: *DAGM-*
472 *Symposium, 2006*, pp. 475–484.

- 473 [26] G. Sandini, M. Tistarelli, Active tracking strategy for monocular depth inference
474 over multiple frames, *IEEE Trans. Pattern Anal. Mach. Intell.* 12 (1) (1990) 13–
475 27.
- 476 [27] F. Woelk, S. Gehrig, R. Koch, A monocular collision warning system, in:
477 Proceedings of the 2nd Canadian Conference on Computer and Robot Vision,
478 2005, pp. 220–227.
- 479 [28] D. Coombs, M. Herman, T. Hong, M. Nashman, Real-time obstacle avoidance
480 using central flow divergence and peripheral flow, in: *IEEE International*
481 *Conference on Computer Vision*, IEEE Computer Society, Los Alamitos, CA,
482 USA, 1995, p. 276.
- 483 [29] C. Colombo, Time to collision from first-order spherical image motion, *Robotics*
484 *and Autonomous Systems* 31 (1-2) (2000) 5–15.
- 485 [30] F. Meyer, Time-to-collision from first-order models of the motion field, *IEEE*
486 *Trans. Robotics and Automation* 10 (1994) 792–798.
- 487 [31] R. C. Nelson, J. Aloimonos, Obstacle avoidance using flow field divergence,
488 *IEEE Trans. Pattern Anal. Mach. Intell.* 11 (10) (1989) 1102–1106.
- 489 [32] J. L. Barron, D. J. Fleet, S. S. Beauchemin, T. A. Burkitt, Performance of
490 optical flow techniques, *International Journal of Computer Vision* 12 (1) (1994)
491 43–77.
- 492 [33] A. Polychronopoulos, M. Tsogas, A. Amditis, L. Andreone, Sensor fusion for
493 predicting vehicles’ path for collision avoidance systems, *IEEE Transactions on*
494 *Intelligent Transportation Systems* 8 (3) (2007) 549–562.
- 495 [34] N. Lazaros, G. C. Sirakoulis, A. Gasteratos, Review of stereo vision algorithms:
496 From software to hardware, *International Journal of Optomechatronics* 2 (4)
497 (2008) 435 – 462.
- 498 [35] R. Laviana, L. Carranza, S. Vargas, G. Linan, E. Roca, A bioinspired
499 vision chip architecture for collision detection in automotive applications,
500 in: R. A. Carmona, G. Linan-Cembrano (Eds.), *Society of Photo-Optical*
501 *Instrumentation Engineers (SPIE) Conference Series*, Vol. 5839, 2005, pp. 13–
502 24.
- 503 [36] J. Cuadri, G. Linan, R. Stafford, M. S. Keil, E. Roca, A bioinspired collision
504 detection algorithm for VLSI implementation, Vol. 5839, SPIE, 2005, pp. 238–
505 248.
- 506 [37] H. Okuno, T. Yagi, Real-time robot vision for collision avoidance inspired by
507 neuronal circuits of insects, in: *IROS*, 2007, pp. 1302–1307.
- 508 [38] H. Okuno, T. Yagi, A visually guided collision warning system with a
509 neuromorphic architecture, *Neural Networks* 21 (10) (2008) 1431–1438.
- 510 [39] R. D. Santer, R. Stafford, F. C. Rind, Retinally-generated saccadic suppression
511 of a locust looming detector neuron: Investigations using a robot locust., *Journal*
512 *of the Royal Society: Interface* 1 (2004) 61–77.

- 513 [40] S. Yue, F. C. Rind, A collision detection system for a mobile robot inspired by
514 the locust visual system, in: ICRA, 2005, pp. 3832–3837.
- 515 [41] S. Yue, F. C. Rind, M. S. Keil, J. Cuadri, R. Stafford, A bio-inspired visual
516 collision detection mechanism for cars: Optimisation of a model of a locust
517 neuron to a novel environment, *Neurocomputing* 69 (13-15) (2006) 1591–1598.